Evolution of an initially turbulent stratified shear layer

Kyle A. Brucker and Sutanu Sarkar

Articles you may be interested in

The statistical evolution of a stratified mixing layer with horizontal shear invoking feature extraction
Phys. Fluids **22**, 115108 (2010); 10.1063/1.3505156

Buoyancy generated turbulence in stably stratified flow with shear
Phys. Fluids **18**, 045104 (2006); 10.1063/1.2193472

Anisotropy of turbulence in stably stratified mixing layers
Phys. Fluids **12**, 1343 (2000); 10.1063/1.870386

Length scales of turbulence in stably stratified mixing layers
Phys. Fluids **12**, 1327 (2000); 10.1063/1.870385

The effect of nonvertical shear on turbulence in a stably stratified medium
Phys. Fluids **10**, 1158 (1998); 10.1063/1.869640

Evolution of an initially turbulent stratified shear layer

Kyle A. Brucker[a)] and Sutanu Sarkar[b)]
*Department of Mechanical and Aerospace Engineering, University of California, San Diego, La Jolla,
California 92093, USA*

Direct numerical simulations of a stratified shear layer are performed for several different values of Reynolds, bulk Richardson, and Prandtl numbers. Unlike previous numerical studies, the initial perturbations are turbulent. These initial broadband perturbations do not allow the formation of distinct coherent structures such as Kelvin-Helmholtz rollers and streamwise vortices found in previous studies. In the absence of stratification, the shear layer thickness grows linearly and fully developed turbulence is achieved with mean velocities, turbulence intensities, and turbulent kinetic energy budgets that agree well with previous experimental and numerical data. When buoyancy is included, the shear layer grows to an asymptotic thickness, and the corresponding bulk Richardson number, Ri_b, is within the range, 0.32 ± 0.06, found in previous studies. The apparent scatter in the evolution of Ri_b is shown to have a systematic dependence on Reynolds and Prandtl numbers. A detailed description of buoyancy effects on turbulence energetics, transport, and mixing is presented. The Reynolds shear stress, $\langle u'_1 u'_3 \rangle$, is significantly reduced by buoyancy, thus decreasing the shear production of turbulence. Owing to buoyancy, gradients in the vertical direction tend to be larger than other gradients in the fluctuating velocity and density fields. However, this anisotropy of the gradients is lower when the Reynolds number increases. Coherent finger-like structures are identified in the density field at late time and their vertical extent obtained by a scaling analysis. © *2007 American Institute of Physics*. [DOI: 10.1063/1.2756581]

I. INTRODUCTION

Buoyancy forces can have a significant stabilizing effect on instabilities and turbulence in shear flows. The suppression of gusts of wind at night, the formation of smog layers in winter, the diurnal cycle of the upper ocean mixed layer, and the collapse of a wake behind a submersible are just a few of many examples of the stabilizing effect of buoyancy. The stratified shear layer between two streams moving with different speeds, the upper fluid being lighter than the lower, is a fundamental problem to study the competition between shear and buoyancy in a controlled setting. This problem has received substantial attention in the published literature and, as shown in the literature survey below, the focus has been primarily on how buoyancy affects instabilities and transition to turbulence. However, there are situations where the shear flow may be initially turbulent, for example, the wake shed of an object at high Reynolds number, and an ocean current of almost constant density that encounters another current below it with a different speed and higher density. The evolution of a shear layer from turbulent initial conditions has not been systematically studied before.

The tilted tube experiments by Thorpe[1–4] were the first laboratory studies of the stratified shear layer. The initial state of quiescent fluid with a two-layer stratification in the experiment corresponded to an initially laminar flow whose subsequent temporal evolution was investigated. Thorpe observed distinct Kelvin-Helmholtz (K-H) billows whose subsequent amalgamation formed a layer of turbulence that initially thickened and mixed the density field. Subsequently, stable vertical density gradients were re-established causing the turbulence to decay most rapidly in the vertical direction, leaving structures with a large aspect ratio in the mixed region. Thorpe also investigated the effect of stratification on the energetics of the flow with particular interest in the fraction of the initial turbulent kinetic energy that may be transferred to turbulent potential energy. The experiments gave a value of final bulk Richardson number in the range of $Ri_{bf} = 0.32 \pm 0.06$. Koop and Browand[5] identified coherent Kelvin-Helmholtz rollers and a braid region in a spatially evolving shear layer. These authors also found a maximum value of bulk Richardson number that is nearly constant ($Ri_{bf} \simeq 0.32$), so long as the initial Richardson number was less than 0.125. Strang and Fernando[6] measured mixing at the sheared density interface between an initially turbulent upper stream and a lower quiescent layer with heavier fluid. The authors found that the initial bulk Richardson number must satisfy $Ri_b > 1.6$ for significant buoyancy effects and satisfy $Ri_b > 2.5$ to extinguish K-H billows. Experimental and numerical studies of a related problem have also been performed, but with the simplification of a uniform density gradient (constant Brunt-Vaisala frequency N) and a uniform shear, S. In contrast to the present case, turbulence is homogeneous and its statistics do not depend on the cross-stream direction. Rohr *et al.*[7] performed the first successful experiments of homogeneous turbulence in a stably stratified shear flow in a salt-stratified water channel. A variation of the initial gradient Richardson number, $Ri_g = N^2/S^2$, led to constant rms vertical velocity fluctuations u'_3 for $Ri = Ri_{cr} = 0.25 \pm 0.05$, growing u'_3 for $Ri < Ri_{cr}$, and decaying u'_3 for

[a)]Electronic mail: kbrucker@ucsd.edu
[b)]Electronic mail: sarkar@ucsd.edu
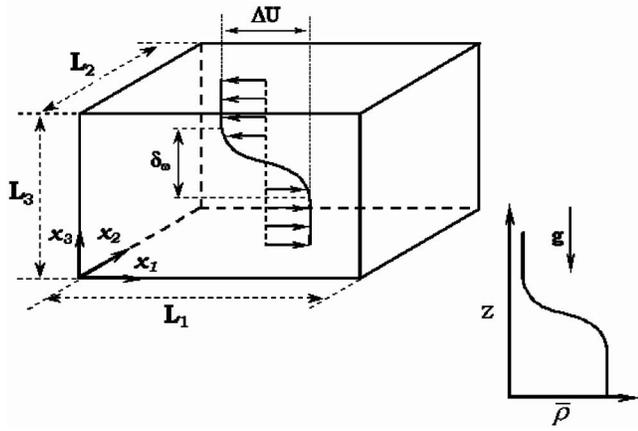
FIG. 1. Schematic of a temporally evolving vertical shear layer, **g**=[0,0,−g].

Ri > Ri$_{cr}$. Piccirillo and Van Atta[8] and Keller and Van Atta[9] investigated the problem using a thermally stratified wind tunnel, examining the detailed velocity and thermal structure.

Numerical studies of the stratified shear layer have also focused on the evolution from small-amplitude disturbances. Early two-dimensional studies[10,11] were followed by three-dimensional DNS,[12–14] albeit at relatively low Re. More recently, Caulfield and Peltier[15] have detailed the evolution during transition to turbulence focusing on the mixing efficiency and the role of secondary instabilities. Smyth and Moum[16,17] give a comprehensive discussion of the formation of K-H billows from small-amplitude initial disturbances, their breakdown to turbulence, the behavior of length scales as well as turbulence anisotropy at small and large scales. They find that the maximum Richardson number is approximately 0.32 in agreement with laboratory experiments. The effect of shear/stratification is known to be important for oceanic mixing at small scales. Smyth et al.[18] have compared measurements of turbulent ocean patches with DNS to aid in the development of models used to predict buoyancy flux from measurements of the dissipation. The situation with uniform shear and uniform stratification has also been studied numerically.[19–25] The critical value, Ri$_{cr}$, of the gradient Richardson number, although found to depend on other parameters such as the Reynolds number and shear number, is found not to violate the stability condition of Ri > 1/4 obtained by linear analysis. The effect of stratification on turbulence energetics, length scales and overturn dynamics have been extensively documented in these numerical studies of uniform shear flow.

We choose to focus our attention on stratified shear flow, schematic in Fig. 1, with the two streams being initially turbulent. The rationale behind this choice is threefold. First, the problem is novel in that there is no published laboratory or DNS data discussing the evolution from turbulent initial conditions. The dynamical effects of stratification on the K-H roll up, amalgamation, and subsequent breakdown have been well studied and those previous efforts need not be repeated here. Second, there are examples of shear flows in nature and in naval applications that are initially turbulent before being subject to significant buoyancy effects. The current simula-

tions are relevant to such flows. Third, the evolution of turbulence statistics and assessment of buoyancy effects in their balance equations are of interest. Such characterization, although available in the uniform shear case, has not been performed in the present case of an inflectional shear layer. The paper is organized as follows: Sec. II details the computational model, initial/boundary conditions, and the simulation parameters. Section III compares the results of an unstratified case with previous numerical and experimental data, and also serves to validate the numerical methodology. Section IV presents the evolution of the bulk Richardson number in the simulations. Section V discusses buoyancy effects on turbulence levels and the influence of initial parameters on these observed effects. Section VI describes the level and anisotropy of the molecular dissipation rates of both velocity and scalar fields. Section VII presents visualizations of the fluctuating vertical vorticity and density fields. Section VIII is on the mixing of the density field and presents statistical measures, and a theoretical discussion of the diffusive-buoyancy scale. Section IX discusses the effects of changes in the initial turbulent perturbations. A summary is given in Sec. X.

II. PROBLEM FORMULATION

A. Model

A schematic depicting the temporally evolving shear layer that develops when two streams of fluid with contrasting densities and velocities are brought together in the presence of a gravitational field is shown in Fig. 1. The velocity streams are of equal magnitude and opposite sign, with the velocity difference across the two streams being ΔU. The model flow evolves temporally in a system with two miscible fluids with density difference $\Delta \rho$. The initial vertical thickness of the mean velocity profile is taken to be equal to that of the mean density profile.

B. Governing equations

The conservation equations for mass, momentum, and scalar for an incompressible, unsteady three-dimensional flow are (here superscript * denotes a dimensional quantity):

Mass:

$$\frac{\partial u_k^*}{\partial x_k^*} = 0; \tag{1}$$

Momentum:

$$\frac{\partial u_i^*}{\partial t^*} + \frac{\partial (u_k^* u_i^*)}{\partial x_k^*} = -\frac{1}{\rho_0}\frac{\partial p^*}{\partial x_i^*} + \nu \frac{\partial^2 u_i^*}{\partial x_k^* \partial x_k^*} - \frac{\rho'^*}{\rho_0}g^* \delta_{i3}; \tag{2}$$

Density:

$$\frac{\partial \rho^*}{\partial t^*} + \frac{\partial (u_k^* \rho^*)}{\partial x_k^*} = \kappa \frac{\partial^2 \rho^*}{\partial x_k^* \partial x_k^*}. \tag{3}$$

The Boussinesq approximation has been employed so that variations in density are ignored except where they give rise to a gravitational force, and p denotes deviations from the

mean hydrostatic pressure. Equations (1)–(3) are nondimensionalized with the velocity difference ΔU, the initial thickness of the shear layer, $\delta_{\omega,0}$, defined as

$$\delta_{\omega,0} \equiv \delta_\omega(t=0); \quad \delta_\omega \equiv \frac{\Delta U}{(d\langle u^*\rangle/dx_3^*)_{max}}, \quad (4)$$

the characteristic density ρ_0, and density difference $\Delta\rho$. With the introduction of these scales, new nondimensional variables are obtained as

$$t = \frac{t^*\Delta U}{\delta_{\omega,0}}, \quad x_i = \frac{x_i^*}{\delta_{\omega,0}}, \quad u_i = \frac{u_i^*}{\Delta U}, \quad \rho' = \frac{\rho'^*}{\Delta\rho}, \quad p = \frac{p^*}{\rho_0\Delta U^2}. \quad (5)$$

After substitution and simplification, the nondimensional equations become

Mass:

$$\frac{\partial u_k}{\partial x_k} = 0; \quad (6)$$

Momentum:

$$\frac{\partial u_i}{\partial t} + \frac{\partial(u_k u_i)}{\partial x_k} = -\frac{\partial p}{\partial x_i} + \frac{1}{Re_0}\frac{\partial^2 u_i}{\partial x_k \partial x_k} - Ri_{b0}\,\rho'\delta_{i3}; \quad (7)$$

Density:

$$\frac{\partial\rho}{\partial t} + \frac{\partial(u_k\rho)}{\partial x_k} = \frac{1}{Re_0 Pr}\frac{\partial^2\rho}{\partial x_k \partial x_k}, \quad (8)$$

where the relevant nondimensional parameters are the initial value of Reynolds number,

$$Re = \frac{\Delta U \delta_\omega}{\nu}, \quad (9)$$

the initial value of the bulk Richardson number,

$$Ri_b = \frac{g\Delta\rho\delta_\omega}{\rho_0\Delta U^2}, \quad (10)$$

and the Prandtl number,

$$Pr = \frac{\nu}{\kappa}. \quad (11)$$

The balance equations for fluctuations with respect to the mean are obtained after applying the following Reynolds decomposition:

$$u_i = \langle u_i\rangle + u_i', \quad \rho = \langle\rho\rangle + \rho', \quad p = \langle p\rangle + p'.$$

The equations governing the turbulent kinetic energy and potential energy are given below.

Turbulent kinetic energy (TKE):

$$\frac{DK}{Dt} = P - \varepsilon + B - \frac{\partial T_i}{\partial x_i}. \quad (12)$$

Here, P is the production of TKE, defined as

$$P \equiv -\langle u_i' u_j'\rangle\frac{\partial\langle u_i\rangle}{\partial x_j} = -\langle u_1' u_3'\rangle\frac{\partial\langle u_1\rangle}{\partial x_3},$$

ε is the dissipation of TKE, defined as

$$\varepsilon \equiv \frac{2}{Re_0}\langle s_{ij}' s_{ij}'\rangle; s_{ij}' = \frac{1}{2}\left(\frac{\partial u_i'}{\partial x_j} + \frac{\partial u_j'}{\partial x_i}\right),$$

$\partial T_i/\partial x_i$ is the transport of TKE, defined as

$$T_i \equiv \frac{1}{2}\langle u_i' u_j' u_j'\rangle + \langle u_i' p'\rangle/\rho_0 - \frac{2}{Re_0}\langle u_j' s_{ij}'\rangle$$

and for, the flow considered, the transport term simplifies to $\partial T_3/\partial x_3$ with

$$T_3 = \frac{1}{2}[\langle u_3' u_1' u_1'\rangle + \langle u_3' u_2' u_2'\rangle + \langle u_3' u_3' u_3'\rangle] + \frac{\langle u_3' p'\rangle}{\rho_0}$$

$$- \frac{2}{Re_0}[\langle u_1' s_{31}'\rangle + \langle u_2' s_{32}'\rangle + \langle u_3' s_{33}'\rangle].$$

B is the buoyancy flux, defined as

$$B \equiv -\frac{g}{\rho_0}\langle\rho' u_3'\rangle.$$

The turbulent potential energy,[26]

$$K_\rho \equiv \frac{g}{2\rho_0}\frac{\langle\rho'^2\rangle}{\partial\langle\rho\rangle/\partial x_3}, \quad (13)$$

is proportional to the density variance whose transport equation is given below.

Density variance:

$$\frac{D}{Dt}\langle\rho'^2\rangle = P_\rho - \frac{\partial}{\partial x_k}T_{\rho k} - \varepsilon_\rho. \quad (14)$$

Here, P_ρ is the production term defined as

$$P_\rho \equiv -2\langle\rho' u_k'\rangle\frac{\partial\langle\rho\rangle}{\partial x_k} = -2\langle\rho' u_3'\rangle\frac{\partial\langle\rho\rangle}{\partial x_3},$$

ε_ρ is the dissipation term defined as

$$\varepsilon_\rho \equiv \frac{2}{PrRe_0}\left\langle\frac{\partial\rho'}{\partial x_k}\frac{\partial\rho'}{\partial x_k}\right\rangle,$$

$\partial T_{\rho k}/\partial x_k$ is the transport term defined by

$$\frac{\partial T_{\rho k}}{\partial x_k} \equiv \frac{\partial}{\partial x_k}\langle\rho'^2 u_k'\rangle - \frac{1}{PrRe_0}\frac{\partial^2}{\partial x_k^2}\langle\rho'^2\rangle$$

$$= \frac{\partial}{\partial x_3}\langle\rho'^2 u_3'\rangle - \frac{1}{PrRe_0}\frac{\partial^2}{\partial x_3^2}\langle\rho'^2\rangle.$$

C. Numerical scheme

A detailed description of the numerical method can be found in Basak.[27] A summary is included here for completeness. Equations (6)–(8) are solved on a staggered grid with normal velocities stored at the cell faces, and density and pressure stored at the cell centers. The spatial discretization is accomplished with a second order central difference
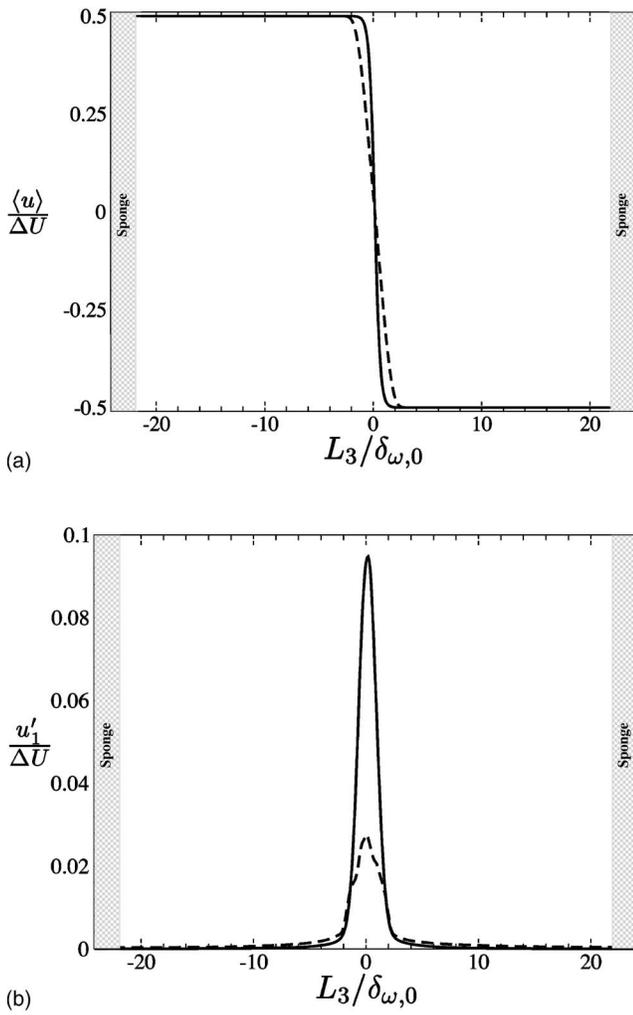
FIG. 2. (a) Mean velocity; (b) fluctuating velocity u_1'. —, initial ($t=0$); –––, final ($t=170$).

scheme, and the temporal integration is performed with a low storage third order Runge-Kutta method. The pressure equation is solved using a multigrid solver. A sponge region is added near the upper and lower boundaries to control spurious reflections from disturbances propagating out of the domain. The sponge layer takes the form of a Rayleigh relaxation function, which is designed in such a way that it gradually relaxes the velocities and density to their respective values at the boundaries. The relaxation term, added in the sponge region to the rhs of Eqs. (7) and (8), is of the form

$$-\phi(x_3)(u_i(x_i,t)-u_{i,\infty}), \tag{15}$$

$$-\phi(x_3)(\rho(x_i,t)-\rho_\infty), \tag{16}$$

where $u_{i,\infty}=[\pm\Delta U/2,0,0]$ and $\rho_\infty=\rho_0\pm\Delta\rho/2$ are, respectively, the free stream velocities and density. The damping function, $\phi(x_3)$, increases quadratically from $\phi=0$ to $\phi=A$ in a region of thickness $a\delta_{\omega,0}$ at the bottom and the top boundaries. Values of $1<a<2$ and $A=10$ have been employed. As can be seen in Fig. 2, a sponge region of $1-2\delta_{\omega,0}$ at the top and bottom boundaries is sufficiently far from the shear layer

during the entire simulation and therefore does not affect the dynamics.

D. Initial conditions

1. Mean

The initial value of the shear layer thickness, along with the fixed values of $\delta_{\omega,0}$, ρ_0, and $\Delta\rho$, are used as follows to define the mean initial conditions

$$\langle u_1\rangle = -\tfrac{1}{2}\tanh(2x_3),$$

$$\langle\rho\rangle = 1 - \frac{\Delta\rho}{2\rho_0}\tanh(2x_3),$$

$$\langle u_2\rangle = \langle u_3\rangle = \langle p\rangle = 0.$$

2. Fluctuations

Broadband fluctuations on the velocity and pressure are imposed as turbulent initial conditions. These broadband fluctuations have an initial spectrum given by

$$E(k) \propto k^4 \exp^{(-2(k/k_0)^2)}, \tag{17}$$

where k_0 is set such that the spectrum peaks at $1.7\delta_{\omega,0}$ and the initial peak intensity of the turbulence is $q^2=\langle u_i'u_i'\rangle =0.03\Delta U^2$. The spectrum is shown in Fig. 3, superimposed is the most unstable mode (by linear instability theory) of $7.23\delta_{\omega,0}$, which would lead to Kelvin-Helmholtz rollers. The extent of the turbulence in the cross-stream direction is dampened exponentially away from the centerline over the thickness of the shear layer. This damping gives a spatial distribution corresponding to a shear layer developing in a quiescent background. The alternate case where the background has a uniform turbulence level will be considered in Sec. IX. The density field was usually initialized to the mean value [i.e., $\rho'(x_i,0)=0$]. The effect of $\rho'(x_i,0)\neq0$ will be discussed in Sec. IX. The strength of the disturbance energy added to the mean flow, $q^2=0.03\Delta U^2$, is not only broadband in nature but significantly stronger than previous studies.[16,17,28] The additional disturbance provides additional kinetic energy that in principle could be converted into potential energy. Thus, the effective or adjusted bulk Richardson number can be defined as

$$\mathrm{Ri}_{bA} = \frac{g\Delta\rho\delta_\omega}{\rho_0(q_r^2+\Delta U^2)}; \quad \text{where } q_r \equiv \frac{1}{2\delta_{\omega,0}}\int_{-\delta_{\omega,0}}^{\delta_{\omega,0}} q^2(x_3)dx_3. \tag{18}$$

If the turbulence was let to develop in an unstratified environment, such that the turbulence intensity reached its stationary value, $q^2=0.04\Delta U^2$, and then subject to stratification the Richardson number defined by Eqs. (10) and (18) differ by only 4.5%. The adjusted Richardson number becomes important when simulations with different levels of initial turbulence or different spatial distributions of turbulence are considered.
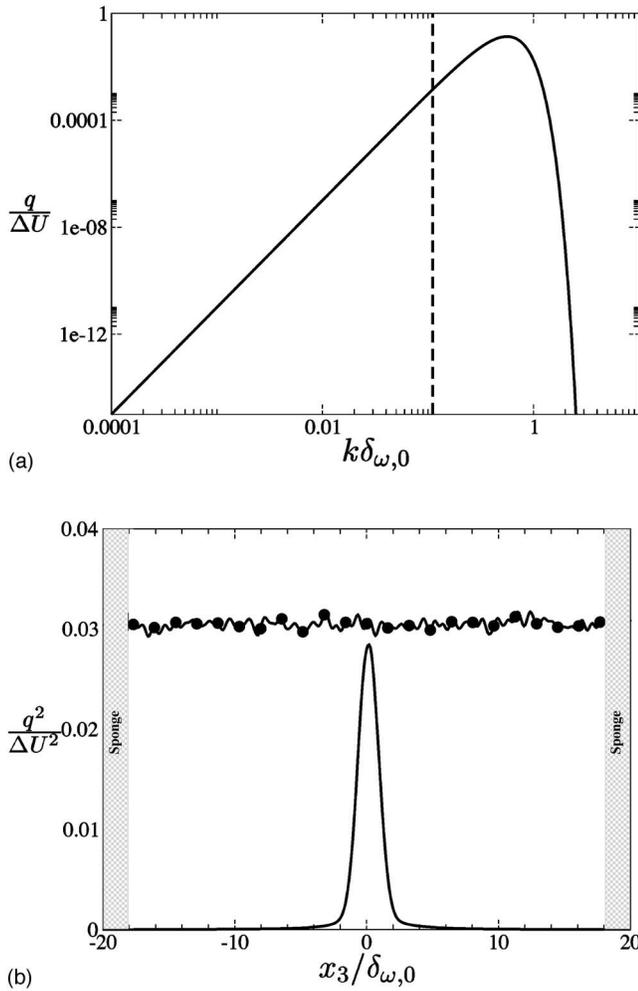
FIG. 3. (a) Spectrum of broadband initial turbulence, —. Most unstable mode by linear instability theory, – – –. (b) Profiles of initial perturbations. —, damped; ●, undamped.

E. Boundary conditions

Periodic boundary conditions are used in the streamwise (x_1) and spanwise (x_2) direction for all variables. In the cross-stream direction (x_3), a combination of Dirichlet and Neumann boundary conditions are used as follows:

$$u_1(0) = \tfrac{1}{2}, \quad u_1(L_3) = -\tfrac{1}{2},$$

$$u_2(0) = u_2(L_3) = 0, \quad p(0) = p(L_3) = 0, \tag{19}$$

$$\frac{\partial u_3}{\partial x_3}(0) = \frac{\partial u_3}{\partial x_3}(L_3) = 0, \quad \frac{\partial \rho}{\partial x_3}(0) = \frac{\partial \rho}{\partial x_3}(L_3) = 0.$$

Recall that a sponge region is also employed at the top and bottom boundaries to minimize the effect of spurious reflections.

F. Simulation parameters

The computational domain $[L_1, L_2, L_3]$, number of computational nodes $[N_1, N_2, N_3]$, grid spacing $[\Delta x_1, \Delta x_2, \Delta x_3]$, initial Reynolds number Re_0, initial Richardson number Ri_{b0}, Prandtl number, initial shear layer thickness $\delta_{\omega,0}$, initial tur-

bulence intensity q, peak wavelength λ_0, minimum and maximum Batchelor scale η_B, and the minimum and maximum values of the diffusive-buoyancy scale $\sqrt{D/N}$ for the simulated cases are reported in Table I.

III. THE UNSTRATIFIED SHEAR LAYER

In the unstratified case, the shear layer approaches a state where its thickness grows linearly while the mean and rms profiles evolve in a self-similar manner. Self-similar behavior has been found in experiments.[31,32] The experimental results are corroborated by DNS.[29,30] The unstratified case V0 simulated here also shows an approach to self-similar behavior. A comparison of case V0 with previous laboratory and DNS data is provided in Figs. 4–6. Figure 4 shows the growth of the momentum thickness, δ_θ, defined as

$$\delta_\theta = \int_{-\infty}^{\infty} \left(\frac{1}{4} - \langle u_1 \rangle^2 \right) dx_3. \tag{20}$$

A consensus of experimental data on the spatially evolving shear layer gives a linear growth of the thickness,

$$\frac{d\delta_\omega}{dx} = C_\delta \frac{U_1 - U_2}{U_1 + U_2} \quad \text{or} \quad \frac{d\delta_\omega}{dt} = 2C_\delta(U_1 - U_2)$$

where

$$\delta_\omega = D_\omega \delta_\theta, \tag{21}$$

with $C_\delta = 0.16$ and $D_\omega = 5$. Figure 4 shows good agreement of case V0 with Eq. (21) as well as the low-Mach number case of Pantano and Sarkar.[29] The terms in the TKE budget were evaluated by averaging the self-similar form at the following times: $t = 48$, 54, 61, 67. A comparison of the TKE budget in the current DNS to that from an incompressible DNS (Ref. 30) and compressible low Mach number DNS (Ref. 29) is given in Fig. 5. Our results agree well with previous DNS data with especially good agreement with the incompressible dataset of Rogers and Moser.[30] Figure 6 compares the Reynolds stresses $R_{ij} = \langle u_i' u_j' \rangle$ obtained here with data from previous studies. The peak streamwise, transverse, and spanwise turbulent intensities, $\sqrt{R_{11}}/\Delta U = 0.17$, $\sqrt{R_{33}}/\Delta U = 0.13$, and $\sqrt{R_{22}}/\Delta U = 0.16$ agree well with previous DNS data. The experimental data show a scatter of about 10% with respect to the simulation data. The shape of the self-similar profiles also agrees well.

In summary, the unstratified case V0 has been successfully benchmarked against previous laboratory and DNS data. In the absence of detailed turbulence measurements in the stratified shear layer, the extensive comparison with unstratified shear layer data serves to validate the numerical tool used here.

IV. BULK RICHARDSON NUMBER

In marked contrast to the evolution of the unstratified shear layer, the growth of the stratified shear layer is bounded by the coupling of the turbulent potential and turbulent kinetic energy. The unstratified shear layer grows linearly in time, see Fig. 4, whereas the stratified counterpart

TABLE I. Flow parameters for simulated cases. Subscripts 0 and f are used to denote the initial and final values. Note that all lengths, velocities, and times are all normalized by the initial shear layer thickness, $\delta_{\omega,0}=0.8$, velocity difference $\Delta U=1$, and $T=\Delta U/\delta_{\omega,0}=1.25$, respectively.

Case	V0	S0	S1	S2	S3	S4	S5	S6	S7	S8	S9	S10	S11
N_1	384	512	384	384	384	384	384	512	384	384	256	512	384
N_2	128	128	128	128	128	128	128	128	128	128	128	128	128
N_3	192	384	512	512	512	512	512	384	512	512	768	384	512
Re_0	640	1280	640	640	640	1280	1280	3200	1280	1280	1280	3200	1280
Ri_{b0}	0.0	0.0	0.1	0.1	0.1	0.1	0.1	0.1	0.05	0.075	0.1	0.1	0.10
Pr	1.0	1.0	0.2	1.0	5.0	0.2	1.0	1.0	1.0	1.0	5.0	0.2	1.0
L_1	64.50	43.00	64.50	64.50	64.50	64.50	64.50	43.00	64.50	64.50	43.00	43.00	64.50
L_2	21.50	10.75	21.50	21.50	21.50	21.50	21.50	10.75	21.50	21.50	21.50	10.75	21.50
L_3	32.25	32.25	48.38	48.38	48.38	48.38	48.38	32.25	48.38	48.38	32.25	32.25	48.38
Δx_1	0.168	0.084	0.168	0.168	0.168	0.168	0.168	0.084	0.168	0.168	0.168	0.084	0.168
Δx_2	0.168	0.084	0.168	0.168	0.168	0.168	0.168	0.084	0.168	0.168	0.168	0.084	0.168
Δx_3	0.168	0.084	0.095	0.095	0.095	0.095	0.095	0.084	0.095	0.095	0.042	0.084	0.095
q	0.03	0.03	0.03	0.03	0.03	0.03	0.03	0.03	0.03	0.03	0.03	0.03	0.03
λ_0	1.79	1.79	1.79	1.79	1.79	1.79	1.79	1.79	1.79	1.79	1.79	1.79	1.79
$(D/N)_{\min}^{(1/2)}$	N/A	N/A	0.160	0.071	0.032	0.113	0.050	0.032	0.061	0.054	0.022	0.031	0.050
$(D/N)_{\max}^{(1/2)}$	N/A	N/A	0.238	0.094	0.039	0.160	0.066	0.044	0.102	0.079	0.029	0.044	0.069
$\eta_{B,\min}$ [a]	0.035	0.010	0.035	0.036	0.017	0.022	0.023	0.011	0.023	0.023	0.010	0.011	0.020
$\eta_{B,\max}$ [b]	0.045	0.016	0.099	0.131	0.056	0.067	0.108	0.020	0.075	0.065	0.079	0.022	0.063
t_f	60	60	150	150	125	150	200	100	350	200	150	115	141
$\delta_{\omega,f}$	5.8	6.6	2.65	2.44	2.15	2.76	2.50	2.51	5.45	3.40	2.43	3.0	2.64
Ri_{bf}	0.0	0.0	0.34	0.29	0.26	0.34	0.31	0.31	0.34	0.31	0.30	0.37	0.33
Re_f	4640	10560	2120	1952	1720	4416	4000	10040	8720	5440	3888	12000	4224

[a] $\eta_{B,\min}=\min(\eta_{\min}, \eta_{\min}Pr^{(-1/2)})$.
[b] $\eta_{B,\max}=\min(\eta_{\max}, \eta_{\max}Pr^{(-1/2)})$.

grows to an asymptotic thickness. Therefore, the bulk Richardson number, Ri_b, defined by Eq. (10), also approaches a constant value, Ri_{bf}. In the literature[4,5,16] it has been found that $Ri_{bf}\simeq0.32\pm0.06$. We have performed simulations (see Table I) systematically varying the initial Richardson, Reynolds, and Prandtl numbers. Figure 7 shows that, in all cases,

$Ri_b(t)$ tends to an asymptotic value. The value of Ri_{bf} varies among cases with all values within the range of 0.32 ± 0.06.

There is a systematic pattern to the seeming scatter in the time evolution among the cases in Fig. 7. If N is increased between cases to change Ri_{b0}, the cases take a shorter time, t,
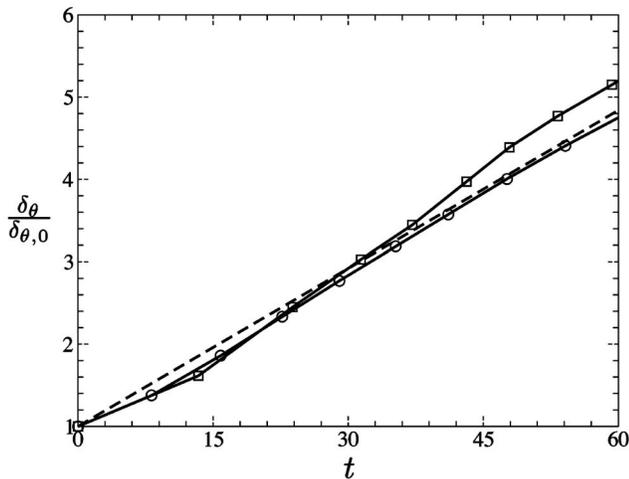
FIG. 4. Comparison of growth of nondimensionalized momentum thickness between current unstratified simulation (V0) and previous DNS of a low Mach number case (Ref. 29). ○, Current DNS; □, Pantano and Sarkar (Ref. 29); ---, Eq. (21).
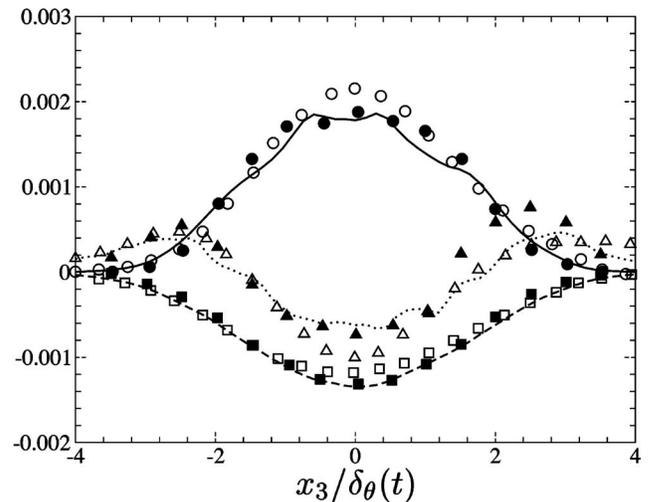
FIG. 5. Turbulent kinetic energy budget. The budget terms are normalized by $\Delta U^3/\delta_\theta$. —, Production (current DNS); - - -, dissipation (current DNS); ⋯, transport (current DNS); ●, production (Ref. 30); ■, dissipation (Ref. 30); ▲, transport (Ref. 30); ○, production (Ref. 29); □, dissipation (Ref. 29); △, transport (Ref. 29).
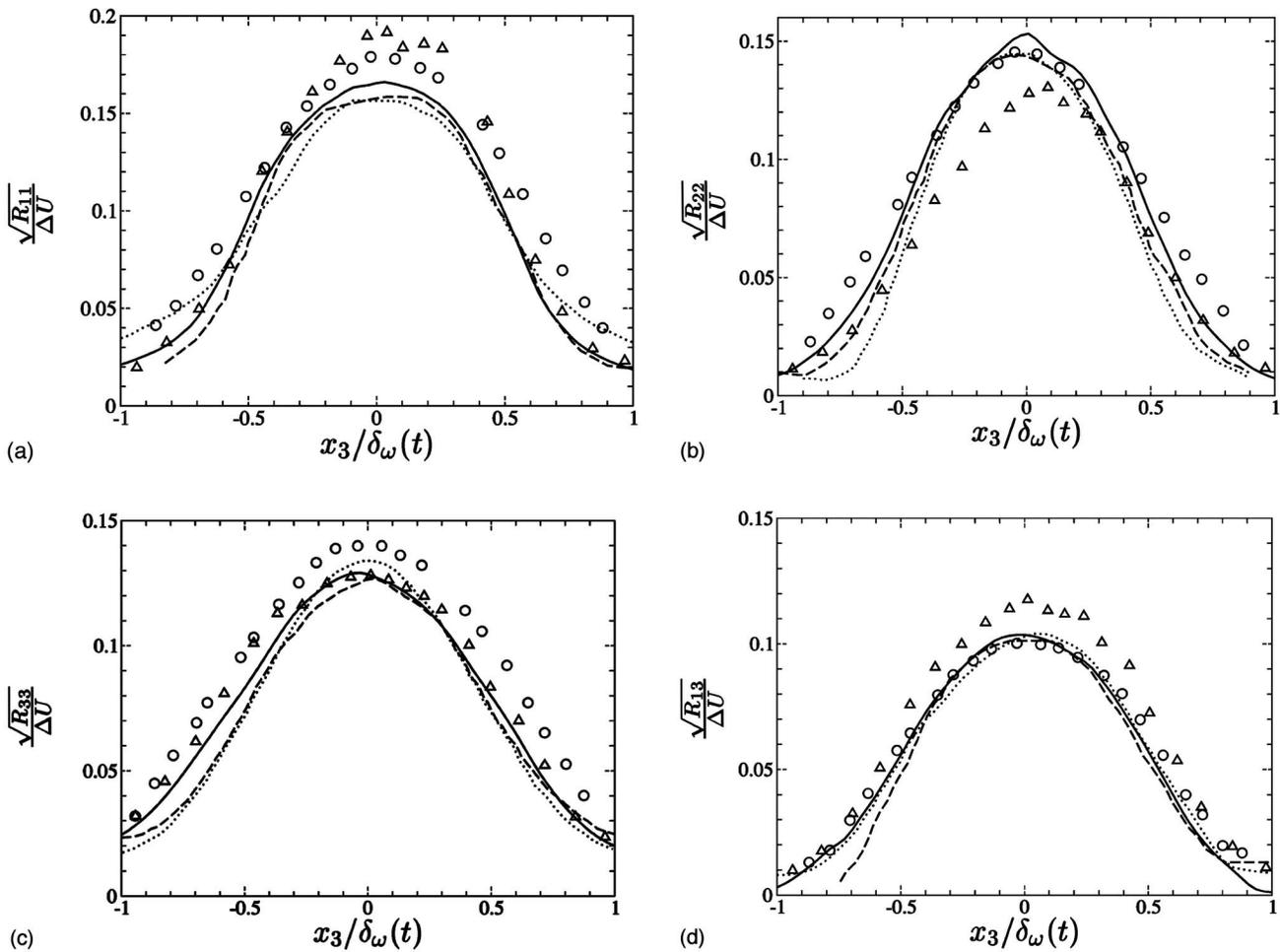
FIG. 6. (a) Streamwise, (b) spanwise, (c) vertical rms velocity, and (d) Reynolds shear stress. —, Current DNS; ···, Pantano and Sarkar (Ref. 29); - - -, Rogers and Moser (Ref. 30); ○, Bell and Mehta (Ref. 31); △, Spencer and Jones (Ref. 32).

to show buoyancy effects. The choice of $\tau_1 = \mathrm{Ri}_{b0}\, t = N_0 \sqrt{\mathrm{Ri}_{b0}}\, t^*$ as nondimensional time, makes the buoyancy term in Eq. (7) invariant with respect to initial stratification. Indeed, examination of the evolution shows that the shear layer reaches its asymptotic thickness at $\tau_1 \simeq 8-10$, see Fig. 7(e). However, the advective terms in the momentum and density transport equations cannot be made invariant using τ_1, precluding τ_1 from completely collapsing the evolution.

The final asymptotic value, Ri_{bf}, also has a marked dependence on the initial parameters. Figure 7(b) shows that Ri_{bf} systematically increases with increasing Reynolds number, and Fig. 7(c) shows that it decreases with increasing Prandtl number. This trend is consistent with the higher Re_0 and lower Pr cases being more energetic as discussed later in Sec. V.

The effect of initial Ri_b, shown in Fig. 7(d), is more subtle. During the initial evolution, the cases with larger Ri_{b0} also have larger $\mathrm{Ri}_b(t)$. However, the stabilizing effect of stratification is also felt earlier by these cases. Thus, the shear layer in S5 essentially stops growing around $t=50$ while the shear layer in case S8 continues growing until $t=100$ to become thicker than that in case S5. Figure 7(e) shows the evolution of Ri_b as a function of τ_1 which, as discussed previously, removes differences in the time re-

quired to reach the final asymptotic state between cases. The final asymptotic state is independent of the initial stratification.

V. TURBULENCE ENERGETICS

Case S5 with $\mathrm{Re}_0 = 1280$, $\mathrm{Pr}=1$ and $\mathrm{Ri}_{b0}=0.1$ will be primarily used to illustrate the effects of stratification on the evolution. The other cases will be discussed, as required, to illustrate the effects of initial parameters on the turbulence. Case S0 has a mean density gradient but, since the buoyancy term is dropped from the momentum equation, the density field behaves like a passive scalar.

In case S0, although the mean velocity and scalar fields evolve indefinitely with time, the turbulence levels, when normalized with ΔU or $\Delta \rho$, reach stationary values. In all the other cases, because of buoyancy effects, not only do the mean profiles cease to thicken, but the turbulent fluctuations, after an initial period of growth, decay monotonically with time. Figure 8(a) shows the differences in the value of center line velocity fluctuations between the stratified case S5 (filled symbols) and the passive scalar case S0. In S5, u_3' decreases at a rate larger than the other velocity components, owing to the explicit coupling to gravity in the u_3 momentum
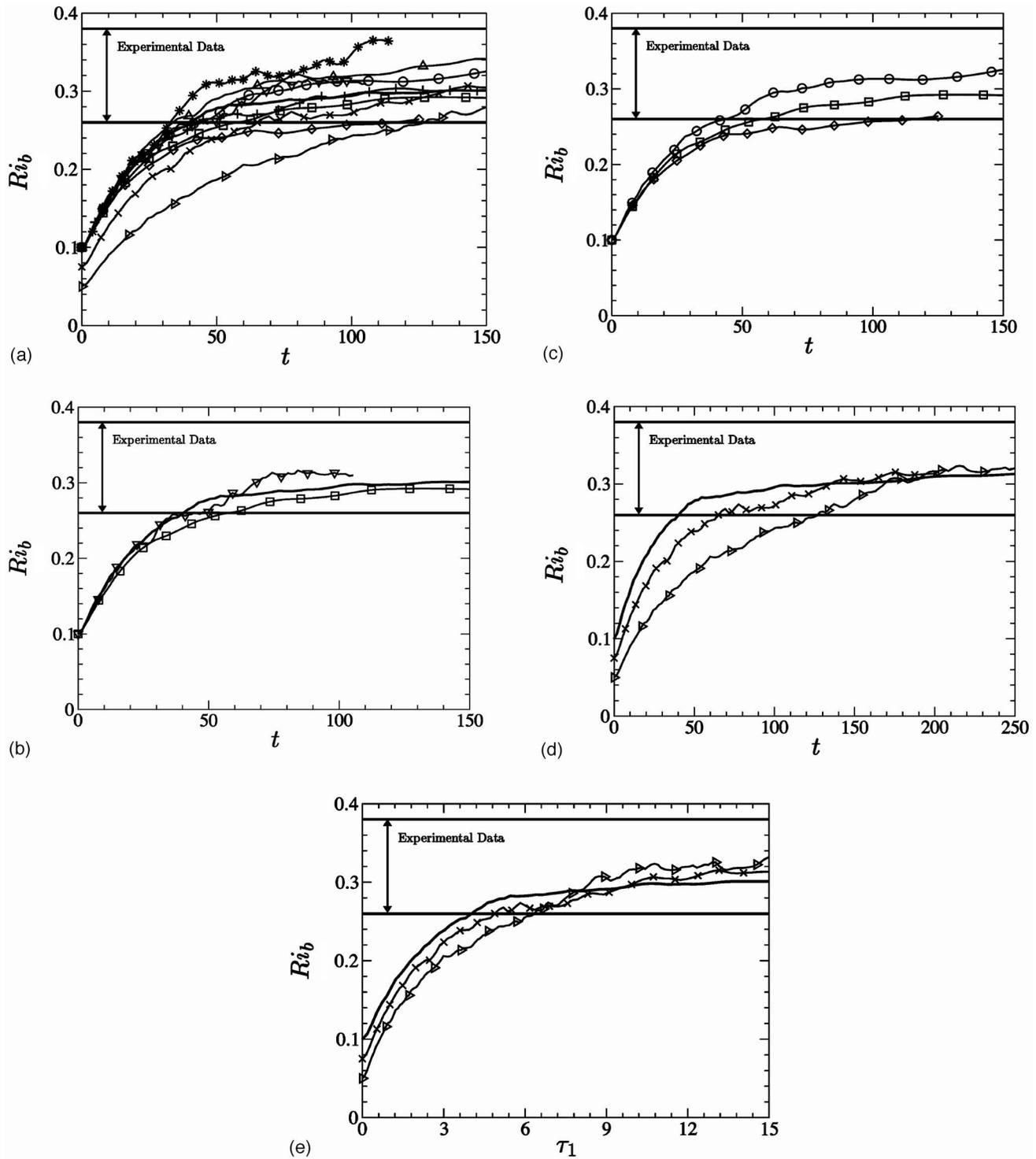
FIG. 7. Bulk Richardson number versus time: (a) all cases; (b) initial Reynolds number effect among cases S2 with $Re_0=640$, S5 with $Re_0=1280$, and S6 with $Re_0=3200$; (c) Prandtl number effect among cases S1 with $Pr=0.2$, S2 with $Pr=1$ and S3 with $Pr=5$; (d) initial Richardson number effect among cases S7 with $Ri_{b0}=0.05$, S8 with $Ri_{b0}=0.075$ and S5 with $Ri_{b0}=0.1$; (e) panel (d) replotted using τ_1 instead of t. ○, (S1); □, (S2); ◇, (S3); △, (S4); —, (S5); ▽, (S6); ▷, (S7); ×, (S8); +, (S9); *, (S10).

equation. The initial increase in u_1' in Fig. 8(a) is due to the increase in the shear production of turbulence. This occurs before the onset of buoyancy effects. Figure 8(b) shows that the density fluctuations which are initially zero, quickly increase in both S0 and S5 to a peak owing to the stirring of the background mean density gradient by the vertical veloc-

ity fluctuations. Although the peak values do not differ much between S0 and S5, the rms density decreases rapidly later in the stratified case because so does u_3'.

Figure 9 shows the following terms in the TKE balance, Eq. (12), evaluated at the centerline: production, dissipation and buoyancy flux. The increase in production between

(a)

FIG. 9. Centerline TKE budget, normalized by $\delta_{\omega,0}/\Delta U^3$, compared between unstratified case S0 and stratified case S5. $\bigcirc$, Unstratified production; $\square$, unstratified dissipation; $\bullet$, stratified production; $\blacksquare$, stratified dissipation; $\blacklozenge$, stratified buoyant flux.

(b)

FIG. 8. (a) Evolution of rms velocity fluctuations on the centerline: $\bigcirc$, u_1' unstratified S0; $\square$, u_2' unstratified S0; $\triangle$, u_3' unstratified S0; $\bullet$, u_1' stratified S5; $\blacksquare$, u_2' stratified S5; $\blacktriangle$, u_3' stratified S5. (b) Evolution of the centerline rms density fluctuations: $\triangle$, passive scalar S0; $\blacktriangle$, stratified S5.

$t=0$ and 5 is consistent with the initial increase in u_1' observed earlier in Fig. 8. In the self-similar unstratified case, the terms in the TKE equation are proportional to $\Delta U^3/\delta_\omega(t)$ and, since δ_ω increases with time, these terms decrease. However, the reduction in turbulent production is much larger in the stratified case. It is worth noting that the buoyancy term is small compared to the production during the time interval (say, $5<t<30$) over which the turbulence intensities have exhibited significant reduction. The main conclusion to be drawn is that the effect of stratification is implicitly felt by the flow; the gravitational term in the momentum equation is not itself a significant sink of turbulent kinetic energy, but rather its presence destroys the correlation of $\langle u_1'u_3'\rangle$ to thereby decrease the shear production of turbulence. This result, obtained here in the situation of inflectional shear, is in agreement with previous studies of uniform shear flow.[19,20,22]

The evolution of turbulence profiles across the shear layer is shown in Fig. 10. During the initial period $0<t<7.5$, not shown here, u_1' increases from its initial value of 0.1 while the shear stress and buoyancy flux increase from their initial zero values. Subsequently, all turbulence intensities and fluxes at the centerline decrease in a monotone fashion. The profiles of rms velocity thicken as a function

of t. The thickening of the shear stress and buoyancy flux profiles is weak because the gradient Richardson number, $\mathrm{Ri}_g=N^2/S^2$, is large and exceeds $\mathrm{Ri}_g=0.25$, in the wings of the shear layer. By $t\simeq70$, the momentum and buoyancy fluxes have decreased to negligible levels and subsequent thickening of the shear layer is due to molecular diffusion.

The effect of Reynolds, Prandtl, and Richardson numbers on the evolution of the rms velocity fluctuations is of interest. Figure 11(a) shows that S6 with a Re=3200 larger than the corresponding value, Re=1280, of S5 has higher u_3'. Examination of other velocity components also indicate that increasing Re makes the turbulence more energetic. This is consistent with previous results from stratified uniform shear flow.[20,22] The lower initial density difference, $\mathrm{Ri}_{b0}=0.05$, in case S7 relative to case S5, also makes the fluctuations more energetic because of smaller ρ' and weaker buoyancy effects at the same value of t. The buoyancy frequency has been proposed in the literature as the characteristic time for measuring stratification. The use of $\tau=\int N_{cl}dt^*$ as dimensionless time in Fig. 11(b) decreases the difference between cases but does not collapse the influence of Ri_{b0}.

The influence of the Prandtl number in Fig. 11(a) is mild but clear; the rms velocity at the centerline decreases from S4 (Pr=0.2) to S5 (Pr=1) to S9 (Pr=5). Case S9 has the smallest value of molecular diffusion of density that leads to the smallest thickening of the density profile owing to molecular diffusion among the cases. Therefore, during the evolution, the value of N_{cl} becomes larger in S9 relative to the other cases and so does the buoyancy effect. Use of the buoyancy time ($\tau=\int N_{cl}dt^*$) in Fig. 11(b) significantly reduces the difference between cases with different Prandtl number.

VI. THE TURBULENT DISSIPATION RATE

The evolution of the molecular dissipation rate, $\int\epsilon dz$, of the velocity field is a measure of the irreversible mixing of the hydrodynamic field. In a self-similarly evolving
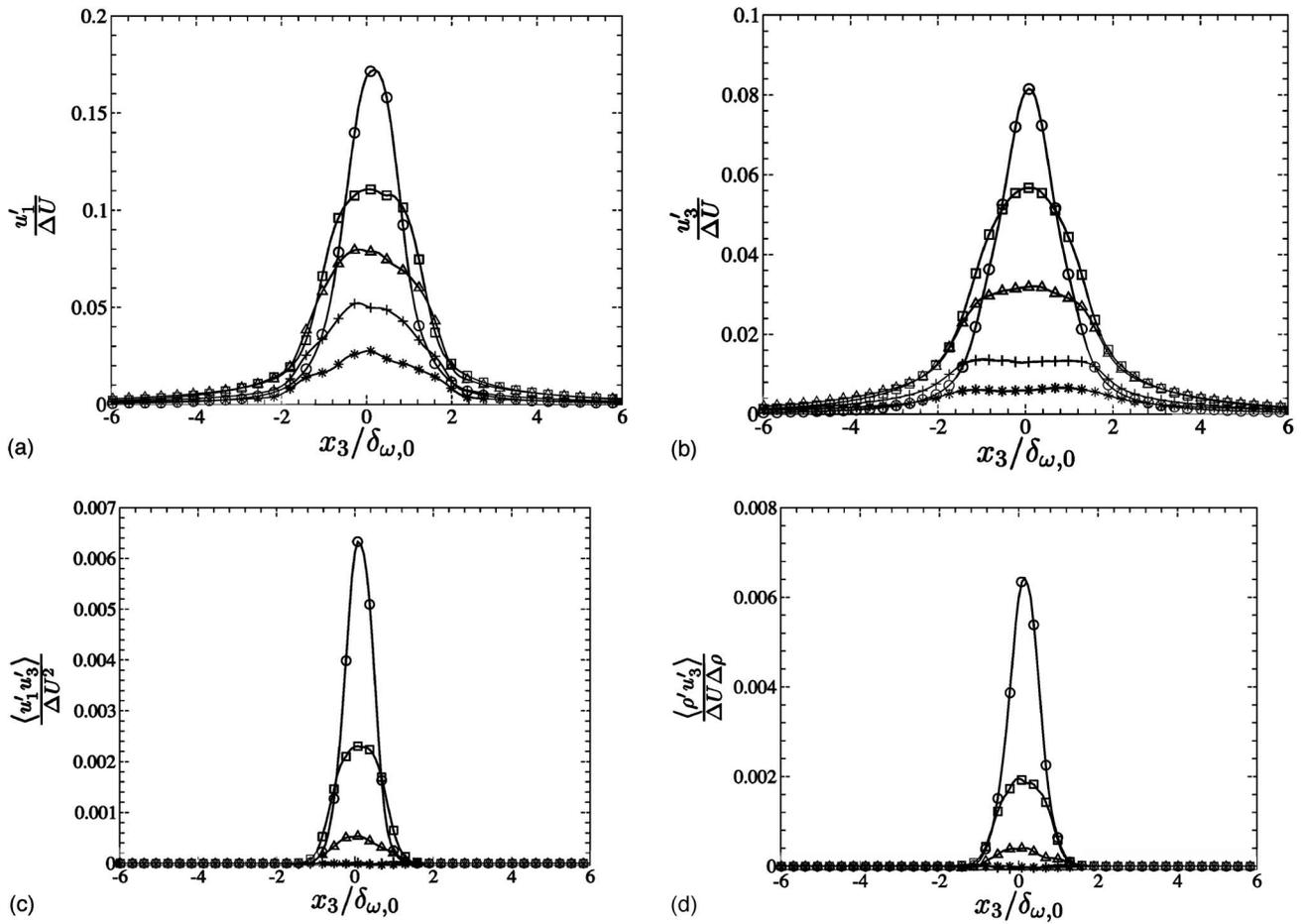
FIG. 10. Turbulence profiles at different times in case S5: (a) u_1', (b) u_3', (c) $\langle u_1'u_3'\rangle$, and (d) $\langle \rho'u_3'\rangle$; $\bigcirc$, $t=7.15$; $\square$, $t=35.94$; $\triangle$, $t=71.71$; $+$, $t=115.65$; $*$, $t=170.73$.

unstratified case, $\epsilon=\int \epsilon\, dz \propto \Delta U^3$. Figure 12(a) shows that $\epsilon \simeq 0.007\Delta U^3$ in case S0. In the stratified cases, ϵ decreases with time. The buoyancy Reynolds number, defined as

$$\mathrm{Re}_B = \frac{\epsilon}{\nu N^2} \qquad (22)$$

has been introduced into the literature as a measure of non-linearity of stratified turbulence. That Re_B is a Reynolds number can be seen by using $\sqrt{\epsilon/N}$ for velocity and the Ozmidov scale, $L_{oz}=\sqrt{\epsilon/N^3}$ for length. The value of dissipation initially increases and, for case S7 ($\mathrm{Ri}_{b0}=0.05$) with the mildest stratification, becomes as large as $\mathrm{Re}_B=150$. Later in time, ϵ decreases and so does Re_B, becoming less than 10 in some of the cases. Therefore, low-Re effects may be anticipated at a later time.

Strongly stratified turbulence with small turbulent Froude number ($u/Nl \ll 1$) can form layers with strong vertical gradients of velocity and density. These layers have been seen visually in grid turbulence,[33–35] in wakes,[36] in Taylor Green vortices,[28] and in a shear layer with horizontal inflectional shear.[37] The statistical signature of layering is that vertical shear dominates other components in the turbulent dissipation rate[37,38] and in the scalar dissipation rate. On the other hand, it is well known that, with increasing Rey-

nolds number, the turbulent dissipation rate becomes more isotropic, and it has been found that anisotropy depends on the value of Re_B.[39]

The preceding discussion motivates us to examine the anisotropy of the dissipation rate. The contribution of the various components of the dissipation rate, ϵ, measured at the centerline are shown for $\mathrm{Re}_0=1280$ (S5) in Fig. 13(a) and for $\mathrm{Re}_0=3200$ (S6) in Fig. 13(b). If isotropic, each of the three diagonal components would contribute 1/15 and each of the six off-diagonal components would contribute 2/15 of the total. The low-Re case deviates strongly from isotropy, especially at late time with the vertical shears $\partial u_1'/\partial x_3$ and $\partial u_2'/\partial x_3$ contributing almost 70% and 20%, respectively. Examination of different cases shows that the contribution of the fluctuating vertical shear component also increases with increasing value of initial stratification, Ri_{b0}. Thus, there is a strong statistical signature of layering in case S5. The effect of increasing the Reynolds number from 1280 to 3200 is shown in Fig. 13(b). There is a large change in the relative contribution of the components. Although the vertical shear components are still larger than the others, they are not as dominant. The other components are closer to the expected isotropic value, especially at early time, $t<20$. At later time,
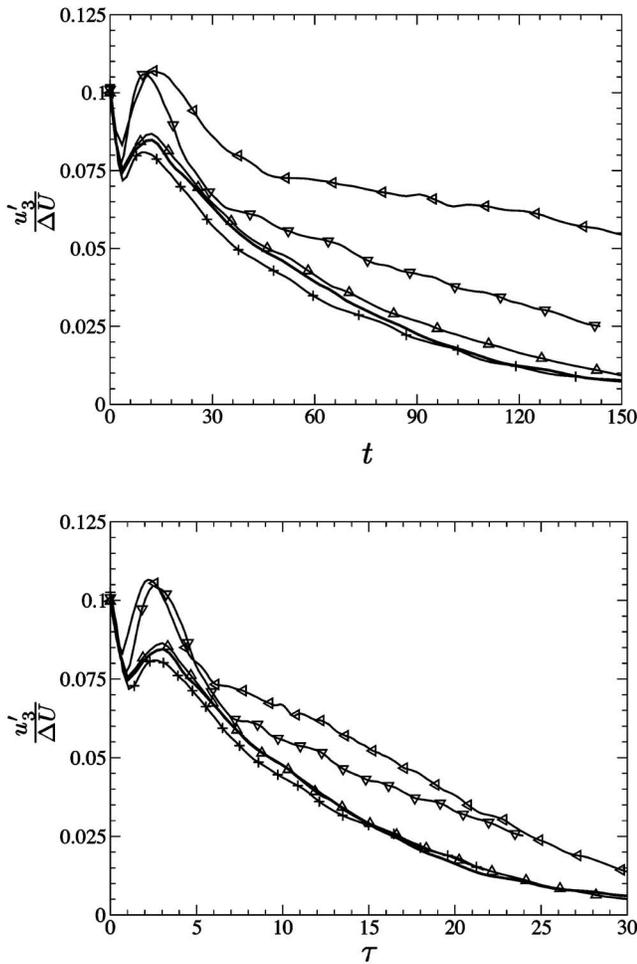
FIG. 11. Evolution of vertical rms velocity (a) using nondimensional time, t, (b) using nondimensional time $\tau = \int N_{cl} dt^*$. $\triangle$, (S4); —, (S5); $\triangledown$, (S6); $\triangleleft$, (S7); $+$, (S9). Case S6 has Re_0 higher than S5, and S7 has Ri_{b0} lower than S5. Cases S4, S5, and S9 have successively increasing Pr.

FIG. 12. (a) Integrated production and dissipation normalized by ΔU^3: $\bullet$, S4; $\blacksquare$, S5; $\blacktriangle$, S6; $\blacktriangleright$, S7; $\blacktriangledown$, S8; $\blacklozenge$, S9; $\blacktriangleleft$, S0. Filled symbols for production, open symbols for dissipation. (b) Buoyancy Reynolds number (symbols as above).

the anisotropy increases because the buoyancy Reynolds number decreases.

The scalar dissipation ϵ_ρ also becomes anisotropic at late time with a preponderance of vertical gradients. In case S5 with $Re_0 = 1280$ (plots not shown), the contribution of the vertical gradient, $\partial \rho' / \partial x_3$ is almost 90% at late time while, in case S6 with $Re_0 = 3200$, it is about 60%.

VII. VISUALIZATIONS

Visualizations of the density field (hot, light fluid in red and cold, heavy fluid in blue) are shown in Fig. 14 at time, $t \simeq 80$. With increasing stratification, the thickness of the mixed layer decreases. The case with no stratification, Figs. 14(a) and 14(b), has interspersed patches of hot and cold fluid with a convoluted interfacial region containing mixed fluid. However, in the case with high initial Ri_b, shown in Figs. 14(c) and 14(d), the flow shows almost no small scale fluctuations in the density field. All that remain are elongated alternating patches of high and low density fluid, subject to mean shear that continue to diffuse into each other. These elongated structure are coherent over the entire spanwise domain [see Fig. 14(d)].

Visualizations of the vorticity field for the unstratified case (V0) have been discussed extensively in Basak and Sarkar[37] (their Fig. 3 and the relevant discussion therein) who conclude that the spatial organization of vorticity at late time is weak. The late time structure is quite complex and different from the flow that develops from infinitesimally small disturbances. There is evidence of discrete lumps of vertical vorticity that grow in time, although the core and braid regions are not distinct. This weak organization of vorticity is consistent with Rogers and Moser.[30] In Fig. 15 the magnitude of the fluctuating vertical vorticity, $|\omega_2'|$, is plotted at $t \simeq 80$ for case S2. When stratification is added there is an organization of the vertical vorticity field into very long streamwise strands that have a significant spanwise extent. This is unlike previous experimental and numerical studies that find the presence of Kelvin-Helmholtz rollers at early time that break down into turbulence.[14,16,18,40,41] It is interesting to note that the late time structures in the fluctuating density and vorticity fields observed here are similar to those found by Smyth and Moum[16] and Smyth et al.[18] who also find elongated streak like structures with significant spanwise

extent in their simulations. The streamwise vorticity field was also visualized. We do not observe the spanwise-periodic organization of streamwise vorticity at late times that was found in previous studies[14,40,41] that had small-amplitude perturbations initially.

VIII. TRANSPORT AND MIXING

A. Diffusive-buoyancy scale

The visualizations of the density field in Figs. 14(e) and 14(f) show that there are coherent mixing regions distinguished by a small vertical scale. In the absence of buoyancy, the lower fluid would be transported up (co-gradient transport). The collapse is due to the buoyancy effect, i.e., the buoyancy term dominates in the u_3-momentum equation,

$$\frac{\partial u_3}{\partial t} + u_j \frac{\partial u_3}{\partial x_j} = -\frac{\partial p'}{\partial x_3} - g\frac{\rho'}{\rho_0} + \nu\frac{\partial^2 u_3}{\partial x_j^2}. \tag{23}$$

The buoyancy term is

$$-g\frac{\rho'}{\rho_0} \sim -\frac{g}{\rho_0}\frac{\partial \langle\rho\rangle}{\partial x_3}L \sim N^2 L, \tag{24}$$

where L is the distance of the fluid parcel to its equilibrium position. The vertical advection term is

$$u_3\frac{\partial u_3}{\partial x_3} \sim \frac{u_3^2}{L}. \tag{25}$$

In the buoyancy-dominated regime, the gravitational term is of the same order as the vertical advection term. Therefore, Eqs. (24) and (25) lead to the following scaling for the vertical strain:

$$\frac{u_3}{L} \sim N. \tag{26}$$

Thus, the density field has diffusive layers subject to a compressive strain N. We now consider the transport equation for the density, specialized to the current case where vertical gradients dominate,

$$\frac{\partial \rho}{\partial t} + u_3\frac{\partial \rho}{\partial x_3} = D\frac{\partial^2 \rho}{\partial x_3^2}. \tag{27}$$

Using Eq. (26) gives $u_3 = N\zeta$, where ζ is a local coordinate from the equilibrium position of the fluid particle. Diffusion ultimately balances advection in the collapsing density microlayers, so that the lower bound for ζ is determined by balancing the second and third terms of Eq. (27),

$$N\zeta\frac{\rho'}{\zeta} \simeq D\frac{\rho'}{\zeta^2}. \tag{28}$$

Hence, the density field has a small vertical scale proportional to the diffusive-buoyancy length scale, l_{DB}, defined by

$$l_{DB} = \sqrt{\frac{D}{N}}. \tag{29}$$

Case S1 shown in Fig. 14(e) has a large diffusive-buoyancy length, $l_{DB} \sim 0.2$ whereas in case S3 shown in Fig.
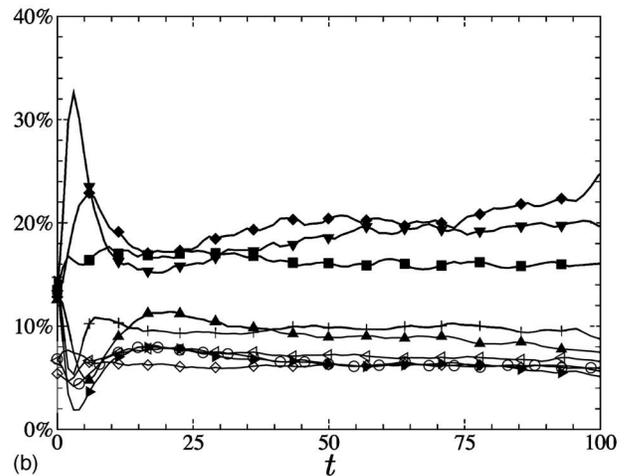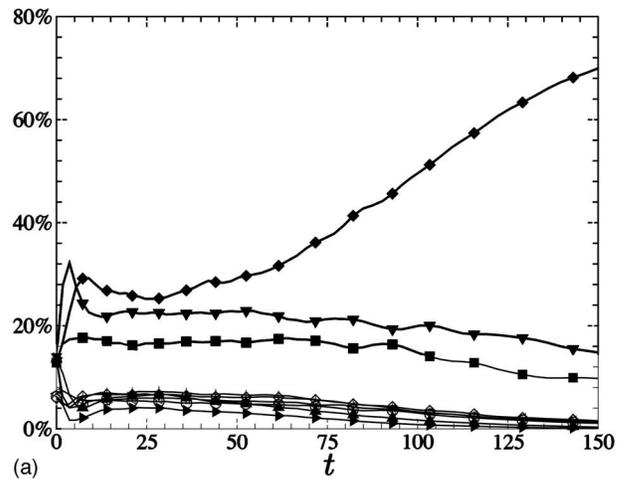
FIG. 13. Components of flow dissipation normalized by $\Delta U^3/\delta_{\omega_0}$. $\mathrm{Ri}_{b,0}$ =0.10 Pr=1, (a) Re_0=1280 (S5), (b) Re_0=3200 (S6). $\bigcirc$, ϵ_{11}; $\blacksquare$, ϵ_{12}; $\blacklozenge$, ϵ_{13}; $\blacktriangle$, ϵ_{21}; $\triangleleft$, ϵ_{22}; $\blacktriangledown$, ϵ_{23}; $\blacktriangleright$, ϵ_{31}; $+$, ϵ_{32}; $\diamond$, ϵ_{33}. Note that $\epsilon_{\alpha\beta}$ denotes the contribution of $\mathrm{Re}_0^{-1}\langle \partial u'_\alpha/\partial x_\beta \partial u'_\alpha/\partial x_\beta\rangle$ to ϵ.

14(f) has a smaller diffusive-buoyancy scale $l_{DB} \sim 0.035$. Clearly, there are thinner vertical structures in Fig. 14(f) when compared to Fig. 14(e).

B. Statistical measures of mixing

The quantity $\Gamma = B/\varepsilon$ is often related to the efficiency of mixing.[18] Here we use the buoyancy transport efficiency[42] which is also related to the flux Richardson number.[43–45] The buoyancy transport efficiency defined below satisfies $0 \leqslant \gamma \leqslant 1$ as long as $-B$ is positive,

$$\gamma = \frac{\int -B dz}{\int (-B + \epsilon) dz}. \tag{30}$$

There has been some objection to the use of γ since the buoyancy flux, a measure of reversible energy transfer between potential and kinetic energy, is not positive definite. Another measure of the mixing efficiency[42] is
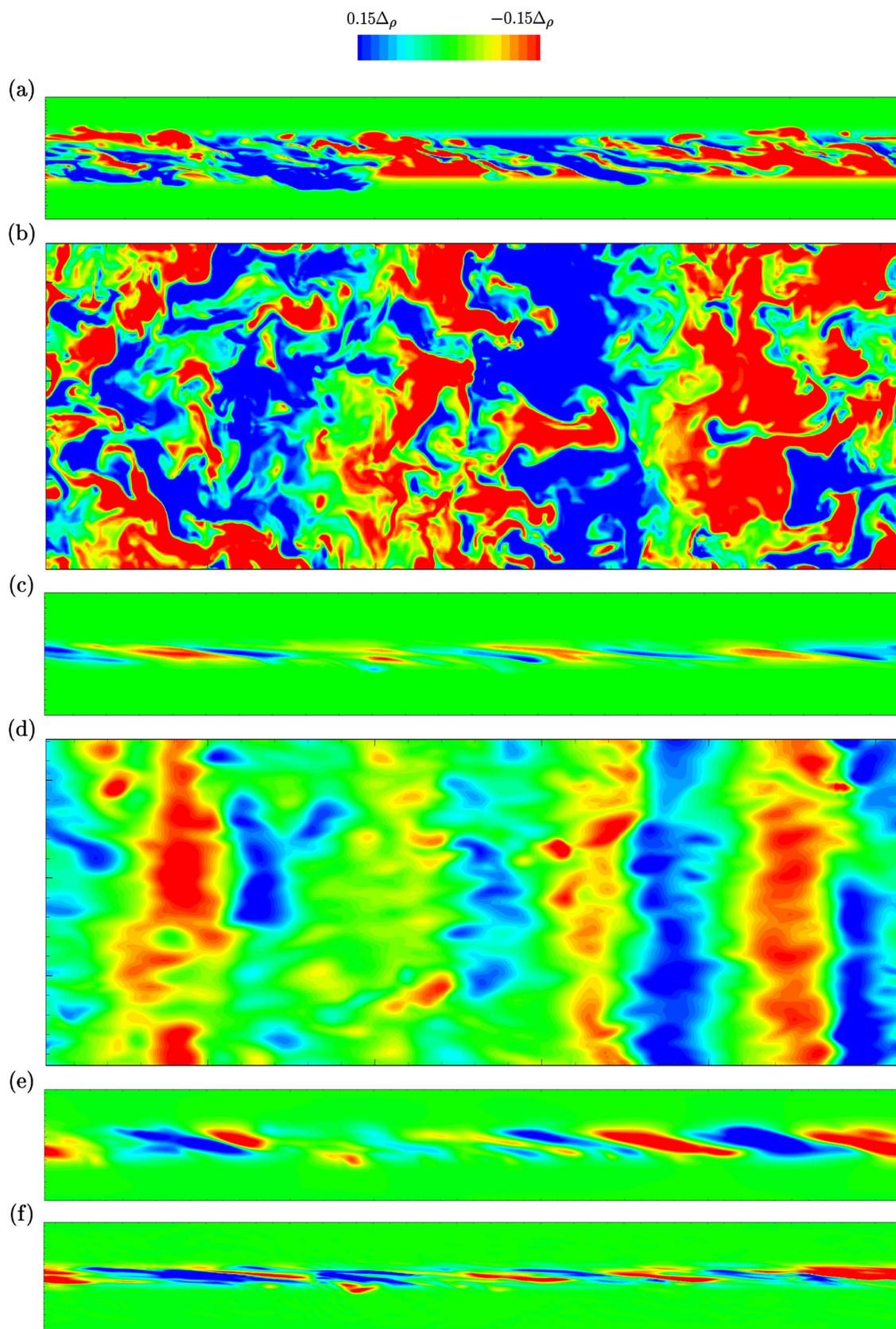
FIG. 14. (Color online) Contour plots of density, $Ri_b=0$ (S0) (a) $L_1\times L_3$ plane at $x_2=L_2/2$; (b) $L_1\times L_2$ plane at $x_3=L_3/2$; $Ri_b=0.10$ (S5); (c) $L_1\times L_3$ plane at $x_2=L_2/2$; (d) $L_1\times L_2$ plane at $x_3=L_3/2$; $Re_0=640$ $L_1\times L_3$ planes at $x_2=L_2/2$; (e) Pr=0.2 (S1); (f) Pr=5 (S3); $t\simeq80$.
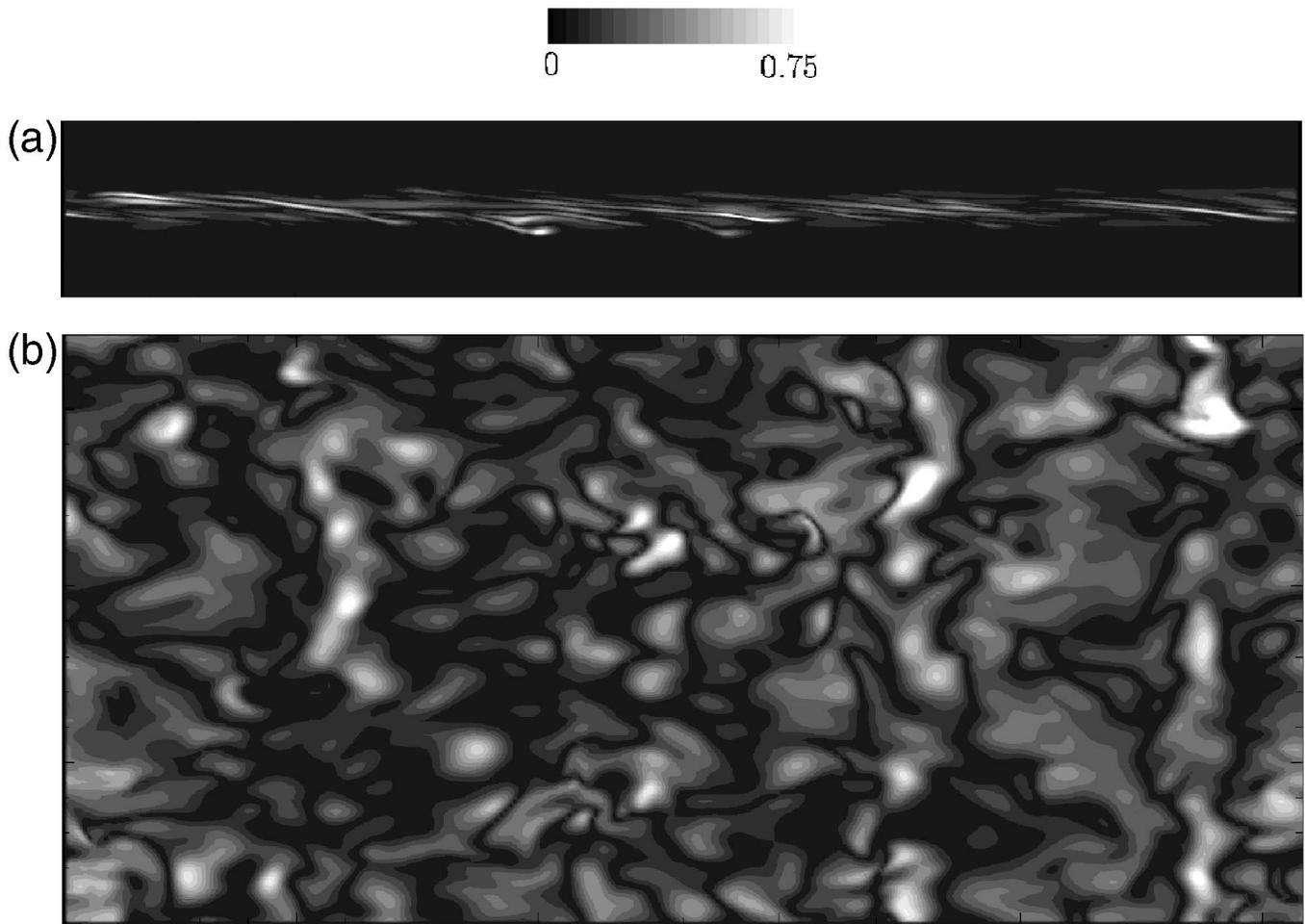
FIG. 15. Contour plots of $|\omega_2'|$ for case S2; (a) $L_1 \times L_3$ plane at $x_2 = L_2/2$, and (b) $L_1 \times L_2$ plane at $x_3 = L_3/2$; $t \simeq 80$.

$$\gamma_d = \frac{\int \epsilon_P dz}{\int (\epsilon_P + \epsilon) dz} \qquad (31)$$

where ϵ_P denotes the molecular dissipation of potential energy. The quantity, γ_d, measures the efficiency of molecular mixing of the buoyancy field relative to that of the velocity field. An alternate definition is based on available potential energy.[46]

Figure 16(a) shows that γ_d evolves to approximately constant values but these values are case-dependent. There is a significant effect of Prandtl number. Cases S9, S5, and S4 have successively smaller Pr or, equivalently, larger value of the heat diffusion coefficient and the value of γ_d is also higher. This trend is corroborated by the results of Smyth et al.[18] who find that in the decay phase $\Gamma \approx 0.2$ for the Pr=2,4,7 number cases, but is larger (0.3–0.4) for the Pr=1 case. There is also a Reynolds number effect: S6 with higher $Re_0 = 3200$ has a higher level of γ_d relative to case S5 with $Re_0 = 1280$.

Figure 16(b) shows the evolution of the buoyancy transport efficiency, γ. Of note is the zero crossing of γ at late time. This occurs because countergradient transport in the wings of the shear layer—a region where the gradient Richardson is large (much larger than the stability criterion of $Ri_g > 0.25$)—cancels the co-gradient transport in the core.

When turbulence is not able to support heavier (lighter) fluid particles that have migrated above (below) their neutral position during the initial stirring phase, these fluid particles return to their neutral location leading to countergradient transport. It is worth noting that the absolute value of B and ϵ are quite small relative to their maximum values when γ crosses zero.

IX. EFFECTS OF TURBULENT INITIAL CONDITIONS

The initial conditions for cases V0–S10 are discussed in Sec. II. The choice of these initial conditions raises two important questions, as previously mentioned in Sec. II. First, how would the evolution change if ambient free-stream turbulence external to the zone of mean shear was allowed in the simulations? Second, what effect does the introduction of finite density fluctuations at $t=0$ have on the evolution? These two questions are addressed below.

A. Ambient free-stream turbulence

The initial undamped profile in Fig. 3(b) is employed as initial conditions for case S11. In contrast to case S5 discussed previously, case S11 has the same initial level of turbulence everywhere in the computational domain. Conse-

FIG. 16. (a) Mixing efficiency, (b) transport efficiency. ●, S4; ■, S5; ▲, S6; ▶, S7; ▼, S8; ◆, S9.

B. Initial density perturbations

Case S5 was rerun with perturbations having amplitude, $\rho'/\Delta\rho=0.14$, added to the mean density. The centerline rms velocity and density fluctuations versus time are shown in Fig. 18. After an initial transient period, $0 \leq t < 10$, the statistics do not show a significant difference for the $\rho'(x_i,0)=0$ and $\rho'(x_i,0) \neq 0$ cases. Riley and de Bruyn Kops[28] arrived at the same conclusion in simulations of stratified turbulence with constant N.

C. Effect on bulk energetics

The effect of changing the initial turbulent conditions on the evolution of bulk Richardson number is examined here. Figure 19(a) shows that the final asymptotic value of Ri_b is almost independent of initial density perturbations. The final value of the bulk Richardson number is somewhat higher for case S11; this is due to the increased kinetic energy present in the initial state. Figure 19(b) shows the evolution of the adjusted bulk Richardson number, Ri_{bA} defined by Eq. (18). The difference between cases S5 and S11 is much less if Ri_{bA} is used instead of Ri_b. In the previous numerical studies,[16] which started with a spectrum that contained most of the "disturbance" energy at the most unstable wavelength, it was also found that Ri_b asymptotes to a value near 0.32, confirming that the energetics are governed by the bulk initial conditions of the flow (ΔU and $\Delta\rho$), and the final state is independent of the details of the motions responsible for the mixing.

X. CONCLUDING REMARKS

The evolution of unstratified and stratified shear layers has been examined using DNS. In the unstratified case our data agree well with previous experimental and numerical studies in terms of turbulence profiles, bulk growth rate, and the turbulent kinetic energy budget. The simulations of the stratified shear layer are started from initially turbulent conditions constructed by adding broadband fluctuations to the mean profile. The presence of stratification causes a significant attenuation of the growth of the shear layer leading to an asymptotic value of bulk Richardson number in the range, $Ri_{bf}=0.32\pm0.06$, found in early experiments and more recent simulations. The lack of a universal asymptotic state is explained by differences in initial Reynolds and Prandtl numbers. The value of Ri_{bf} decreases with increasing Prandtl number and increases with increasing initial Reynolds number. The effect of initial stratification is characterized by the choice of $\tau_1=N_0 t^* \sqrt{Ri_{b0}}$. Although a complete collapse is not possible in the preasymptotic regime, the choice of τ_1 does show that Ri_{bf} is reached by $\tau_1 \simeq 10$, independent of Ri_{b0}. The cross-stream profile and initial spectrum of the perturbations does not effect the bulk dynamics of the system. The asymptotic value of Ri_b is independent of temporal characteristics of the mixing (the formation of K-H rollers and their subsequent breakdown seen in previous studies that start with small-amplitude perturbations versus intense small-scale perturbations in the present case).

As in studies of the uniform shear case, we find that the

quently, the dynamics outside the shear layer are clearly different between cases S5 and S11 as shown in Fig. 10. However, the evolution of the statistics *inside* the shear layer is similar between both cases. Comparing the streamwise rms velocity u_1' shown in Figs. 10(a) and 17(a), case S11 has peak values about 20% higher than in case S5. This is not surprising considering that the initial turbulent kinetic energy integrated over the initial shear layer thickness is 40% higher in case S11. At late times the profile becomes multi-inflectional, behavior that is not seen in case S5. Comparing the cross-stream rms velocity u_3' shown in Figs. 10(b) and 17(b) the multi-inflectional profile is even more evident. Both cases show strongly reduced u_3' in the shear layer, but case S11 has substantial u_3' fluctuations outside the shear layer that persist to late times ($t>100$). In case S5 where the initial fluctuations were damped to zero outside the shear layer, u_3' fluctuations remain small in the external region. Even though the rms velocities behave differently, the turbulent fluxes, $\langle u_1'u_3'\rangle$ and $\langle\rho'u_3'\rangle$, behave similarly. Figures 10(c), 10(d), 17(c), and 17(d), respectively, show similar temporal evolution, with negligible turbulent transport at late time, $t>100$.

FIG. 17. Turbulence profiles at different times in case S11: (a) u_1', (b) u_3', (c) $\langle u_1' u_3' \rangle$, and (d) $\langle \rho' u_3' \rangle$. $\bigcirc$, $t = 6.87$; $\square$, $t = 36.39$; $\triangle$, $t = 71.74$; $+$, $t = 115.28$.

buoyancy flux itself is not a significant sink in the budget of turbulent kinetic energy. Rather, it reduces the correlation $\langle u_1' u_3' \rangle$ thus reducing the shear production of turbulence. This reduction in the sustaining mechanism leads to a significant reduction in the turbulence velocity and density fluctuations. The vertical component, u_3', decreases more rapidly due to

FIG. 18. Evolution of rms velocities and density: $\bigcirc$, u_1'; $\square$, u_2'; $\triangle$, u_3'; $\diamond$, ρ'. Open symbols $\rho'(x_i, t) \neq 0$, and closed symbols $\rho'(x_i, t) = 0$.

the explicit coupling to gravity in the u_3 momentum equation. Although the velocity fluctuations spread outside the thickness of the initial shear layer, see Figs. 10(a) and 10(b), the momentum and buoyancy fluxes $\langle u_1' u_3' \rangle$ and $\langle \rho' u_3' \rangle$ spread little if at all outside the confines of the initial shear layer $\pm \delta_{\omega,0}$ even for moderate initial stratification, $Ri_{b0} = 0.1$.

The larger the initial Reynolds number or the lower the initial stratification, the more energetic the fluctuations are at a given time. The effect of the Prandtl number at a given time is collapsed by the choice of $\tau = \int N_{CL} dt^*$. If this choice is not made, the strength of the fluctuations decreases somewhat with increasing Prandtl number.

The anisotropy in the velocity and scalar dissipation rates tends toward the expected isotropic values as the initial Reynolds number increases. At late times, as the turbulence becomes weak compared to its maximum value, the components of dissipation again become more anisotropic, albeit less so at high Re_0. This increase in the anisotropy of the dissipation at late time is symptomatic of layering. The vertical extent of these layers is obtained through a scaling analysis resulting in a diffusive-buoyancy length scale, $l_{DB} = \sqrt{D/N}$. Finally, we find that the use of the transport efficiency, γ, as a surrogate for the mixing efficiency, γ_d, may be

FIG. 19. (a) Bulk Richardson number versus time: $---$, S5 with Re_0 =1280, Pr=1, Ri_{b0}=0.10; $---$, (S11) with uniform fluctuations; $\cdots$, $\rho'(x_i,t)\neq0$. (b) Adjusted bulk Richardson number, (18). —, S5; $---$, S11.

misleading at late times when significant countergradient transport can lead to negative values of γ.

ACKNOWLEDGMENTS

[1] S. A. Thorpe, "A method of producing a shear flow in a stratified fluid," J. Fluid Mech. **32**, 693 (1968).

[2] S. A. Thorpe, "Experiments on the instability of stratified shear flows: Miscible fluids," J. Fluid Mech. **46**, 299 (1971).

[3] S. A. Thorpe, "Experiments on instability and turbulence in a stratified shear flow," J. Fluid Mech. **61**, 731 (1973).

[4] S. A. Thorpe, "Turbulence in stably stratified fluids: A review of laboratory experiments," Boundary-Layer Meteorol. **5**, 95 (1973).

[5] C. G. Koop and F. K. Browand, "Instability and turbulence in a stratified fluid with shear," J. Fluid Mech. **93**, 135 (1979).

[6] E. J. Strang and H. J. S. Fernando, "Entrainment and mixing in stratified shear flows," J. Fluid Mech. **428**, 349 (2001).

[7] J. J. Rohr, E. C. Itsweire, K. N. Helland, and C. W. Van Atta, "Growth and decay of turbulence in a stably stratified shear flow," J. Fluid Mech. **195**, 77 (1988).

[8] P. Piccirillo and C. W. Van Atta, "The evolution of a uniformly sheared thermally stratified turbulent flow," J. Fluid Mech. **334**, 61 (1997).

[9] K. H. Keller and C. W. Van Atta, "An experimental investigation of the vertical temperature structure of homogeneous stratified shear turbulence," J. Fluid Mech. **425**, 1 (2000).

[10] P. C. Patnaik, F. S. Sherman, and G. M. Corcos, "A numerical simulation of Kelvin-Helmholtz waves of finite amplitude," J. Fluid Mech. **73**, 215 (1976).

[11] G. P. Klaassen and W. R. Peltier, "Evolution of finite amplitude Kelvin-Helmholtz billows in two spatial dimensions," J. Atmos. Sci. **42**, 1321 (1985).

[12] C. Staquet and J. J. Riley, "A numerical study of a stably-stratified mixing layer," in *Turbulent Shear Flows 6* (Springer-Verlag, Berlin, 1989), pp. 381–397.

[13] G. P. Klaassen and W. R. Peltier, "The influence of stratification on secondary instability in free shear layers," J. Fluid Mech. **227**, 71 (1991).

[14] C. P. Caulfield and W. R. Peltier, "Three dimensionalization of the stratified mixing layer," Phys. Fluids **6**, 3803 (1994).

[15] C. P. Caulfield and W. R. Peltier, "The anatomy of the mixing transition in homogeneous and stratified free shear layers," J. Fluid Mech. **413**, 1 (2000).

[16] W. D. Smyth and J. N. Moum, "Length scales of turbulence in stably stratified mixing layers," Phys. Fluids **12**, 1327 (2000).

[17] W. D. Smyth and J. N. Moum, "Anisotropy of turbulence in stably stratified mixing layers," Phys. Fluids **12**, 1343 (2000).

[18] W. D. Smyth, J. N. Moum, and D. R. Caldwell, "The efficiency of mixing in turbulent patches: Inferences from direct simulations and microstructure observations," J. Phys. Oceanogr. **31**, 1969 (2001).

[19] T. Gerz, U. Schumann, and S. E. Elghobashi, "Direct numerical simulation of stratified homogeneous turbulent shear flows," J. Fluid Mech. **200**, 563 (1989).

[20] S. E. Holt, J. R. Koseff, and J. H. Ferziger, "A numerical study of the evolution and structure of homogeneous stably stratified sheared turbulence," J. Fluid Mech. **237**, 499 (1992).

[21] H. J. Kaltenbach, T. Gerz, and U. Schumann, "Large-eddy simulation of homogeneous turbulence and diffusion in stably stratified shear flow," J. Fluid Mech. **280**, 1 (1994).

[22] F. G. Jacobitz, S. Sarkar, and C. W. Van Atta, "Direct numerical simulations of the turbulence evolution in a uniformly sheared and stably stratified flow," J. Fluid Mech. **342**, 231 (1997).

[23] F. G. Jacobitz and S. Sarkar, "A direct numerical study of transport and anisotropy in a stably stratified turbulent flow with uniform horizontal shear," Flow, Turbul. Combust. **63**, 343 (2000).

[24] L. H. Shih, J. R. Koseff, J. H. Ferziger, and C. R. Rehmann, "Scaling and parameterization of stratified homogeneous turbulent shear flow," J. Fluid Mech. **412**, 1 (2000).

[25] P. J. Diamessis and K. K. Nomura, "The structure and dynamics of overturns in stably stratified homogeneous turbulence," J. Fluid Mech. **499**, 197 (2004).

[26] E. C. Itsweire, J. R. Koseff, D. A. Briggs, and J. H. Ferziger, "Turbulence in stratified shear flows: Implications for interpreting shear-induced mixing in the ocean," J. Phys. Oceanogr. **23**, 1508 (1993).

[27] S. Basak, "Dynamics of stratified shear layers with horizontal shear," Ph.D. thesis, University of California, San Diego, La Jolla, California, 2005.

[28] J. J. Riley and S. M. de Bruyn Kops, "Dynamics of turbulence strongly influenced by buoyancy," Phys. Fluids **15**, 2047 (2003).

[29] C. Pantano and S. Sarkar, "A study of compressibility effects in the high-speed turbulent shear layer using direct simulation," J. Fluid Mech. **451**, 329 (2002).

[30] M. M. Rogers and R. D. Moser, "Direct simulation of a self-similar turbulent mixing layer," Phys. Fluids **6**, 903 (1994).

[31] J. H. Bell and R. D. Mehta, "Development of a two-stream mixing layer from tripped and untripped boundary layers," AIAA J. **28**, 2034 (1990).

[32] B. W. Spencer and B. G. Jones, "Statistical investigation of pressure and velocity fields in the turbulent two-stream mixing layer," AIAA Pap. 71-613 (1971).

[33] A. M. Fincham, T. Maxworthy, and G. R. Spedding, "Energy dissipation and vortex structure in freely decaying, stratified grid turbulence," Dyn. Atmos. Oceans **23**, 155 (1996).

[34] O. Métais and J. R. Herring, "Numerical simulations of freely evolving

turbulence in stably stratified fluids," J. Fluid Mech. **202**, 117 (1989).

[35] Y. Kimura and J. R. Herring, "Diffusion in stably stratified turbulence," J. Fluid Mech. **328**, 253 (1996).

[36] G. R. Spedding, "The streamwise spacing of adjacent coherent structures in stratified wakes," Phys. Fluids **14**, 3820 (2002).

[37] S. Basak and S. Sarkar, "Dynamics of a stratified shear layer with horizontal shear," J. Fluid Mech. **568**, 19 (2006).

[38] F. G. Jacobitz and S. Sarkar, "On the shear number effect in stratified shear flow," Theor. Comput. Fluid Dyn. **13**, 171 (1999).

[39] D. A. Hebert and S. M. de Bruyn Kops, "Relationship between vertical shear rate and kinetic energy dissipation rate in stable stratified flows," Geophys. Res. Lett. **33**, 3069 (2006).

[40] Y. D. Afanasyev and W. R. Peltier, "The three-dimensionalization of stratified flow over two-dimensional topography," J. Atmos. Sci. **55**, 19 (1998).

[41] S. A. Thorpe, "Laboratory observations of secondary structures in Kelvin-Helmholtz billows and consequences for ocean mixing," Geophys. Astrophys. Fluid Dyn. **34**, 175 (1985).

[42] W. R. Peltier and C. P. Caulfield, "Mixing efficiency in stratified shear flows," Annu. Rev. Fluid Mech. **35**, 135 (2003).

[43] G. N. Ivey and J. Imberger, "On the nature of turbulence in a stratified fluid. Part I: The energetics of mixing," J. Phys. Oceanogr. **21**, 650 (1991).

[44] A. A. Townsend, "The effects of radiative transfer on turbulent flow of a stratified fluid," J. Fluid Mech. **4**, 361 (1958).

[45] J. J. Rohr, E. C. Itsweire, and C. W. Van Atta, "Mixing efficiency in stably-stratified decaying turbulence," Geophys. Astrophys. Fluid Dyn. **29**, 221 (1984).

[46] K. B. Winters and E. A. D'Asaro, "Diascalar flux and the rate of fluid mixing," J. Fluid Mech. **317**, 179 (1996).